

pubs.acs.org/JPCB Article

Vibrational Energy Landscapes and Energy Flow in GPCRs

Published as part of The Journal of Physical Chemistry B virtual special issue "Richard J. Saykally Festschrift". Humanath Poudel, David J. Wales,* and David M. Leitner*



Cite This: J. Phys. Chem. B 2024, 128, 7568-7576



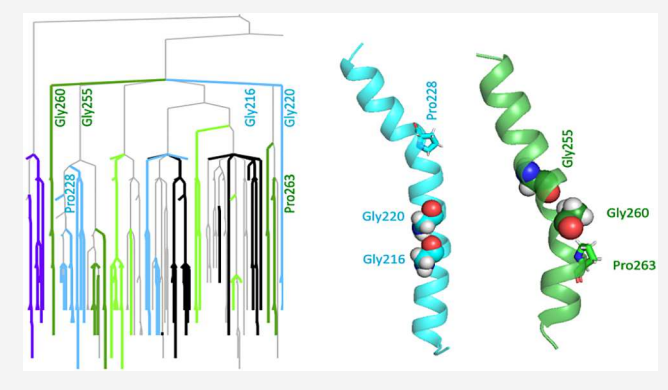
ACCESS

III Metrics & More

Article Recommendations

Supporting Information

ABSTRACT: We construct and analyze disconnectivity graphs to provide the first graphical representation of the vibrational energy landscape of a protein, in this study β_2AR , a G-protein coupled receptor (GPCR), in active and inactive states. The graphs, which indicate the relative free energy of each residue and the minimum free energy barriers for energy transfer between them, reveal important composition, structural and dynamic properties that mediate the flow of energy. Prolines and glycines, which contribute to GPCR plasticity and function, are identified as bottlenecks to energy transport along the backbone from which alternative pathways for energy transport via nearby noncovalent contacts emerge, seen also in the analysis of first passage time (FPT) distributions presented here. Striking differences between the disconnectivity graphs and FPT distributions for the inactive and



disconnectivity graphs and FPT distributions for the inactive and active states of β_2 AR are found where structural and dynamic changes occur upon activation, contributing to allosteric regulation.

1. INTRODUCTION

Recent ultrafast time-resolved IR^{1,2} and Raman³⁻⁶ spectroscopic studies can map the flow of vibrational energy in proteins at the level of individual amino acids. These investigations build on earlier experiments and modeling 1-25 to provide a more detailed description of the anisotropic flow of energy following chemical reactions or photoexcitation. The study of energy flow in proteins is motivated by the central role this process plays in chemical reaction dynamics and kinetics. Thermal excitation, e.g., of dynamically coupled residues of dihydrofolate reductase at sites distal to the enzyme-substrate binding region, can accelerate enzyme catalysis, 30 and hydrogen tunneling in lipoxygenases is activated by vibrational energy flow through an extensive network of residues.^{31–33} Vibrational cooling following ligand dissociation in heme proteins rapidly stabilizes the product conformer, ¹⁸⁻²² as does vibrational cooling following photoisomerization in rhodopsin, a G-protein coupled receptor (GPCR).³⁴⁻³⁶ Vibrational energy flow is related not only to protein structure but also structural dynamics, so that measurements can provide information about dynamics during protein function. Rates of vibrational energy transfer across noncovalent contacts depend on dynamics, so that changes upon ligand binding contributing to allostery can be detected from measurement of energy transfer rates. 37-41 Current efforts in the computational design of protein receptors and allosteric drug development 42 can thus benefit from a more detailed understanding of energy flow in GPCRs.

In this contribution, we construct the first disconnectivity graph 43,44 analysis that illustrates the relative free energies and minimum energy barriers between residues governing the flow of vibrational energy in a protein. We examine disconnectivity graphs for the β_2 adrenergic receptor (β_2 AR), a GPCR, in its inactive and active states. The graphs reveal bottlenecks to energy flow along parts of the main chain, which until now have not been identified in any protein, and the emergence of alternative energy flow pathways via noncovalent contacts, located near the bottlenecks along the main chain. They also report on the consequences of rearrangement of noncovalent contacts in the transition from the inactive to the active state, as well as changes in contact dynamics upon change in state, which contribute to allostery.

 β_2 AR is a membrane-bound, rhodopsin-like GPCR found in smooth muscle cells, and mediates many physiological responses, including smooth muscle relaxation and bronchodilation. As β_2 AR is not only of interest in the study of signaling and communication in cells, but also a receptor that is the target of pharmacologists and drug developers for the treatment of asthma and cardiac diseases. There has been

Received: July 5, 2024
Revised: July 16, 2024
Accepted: July 17, 2024
Published: July 26, 2024





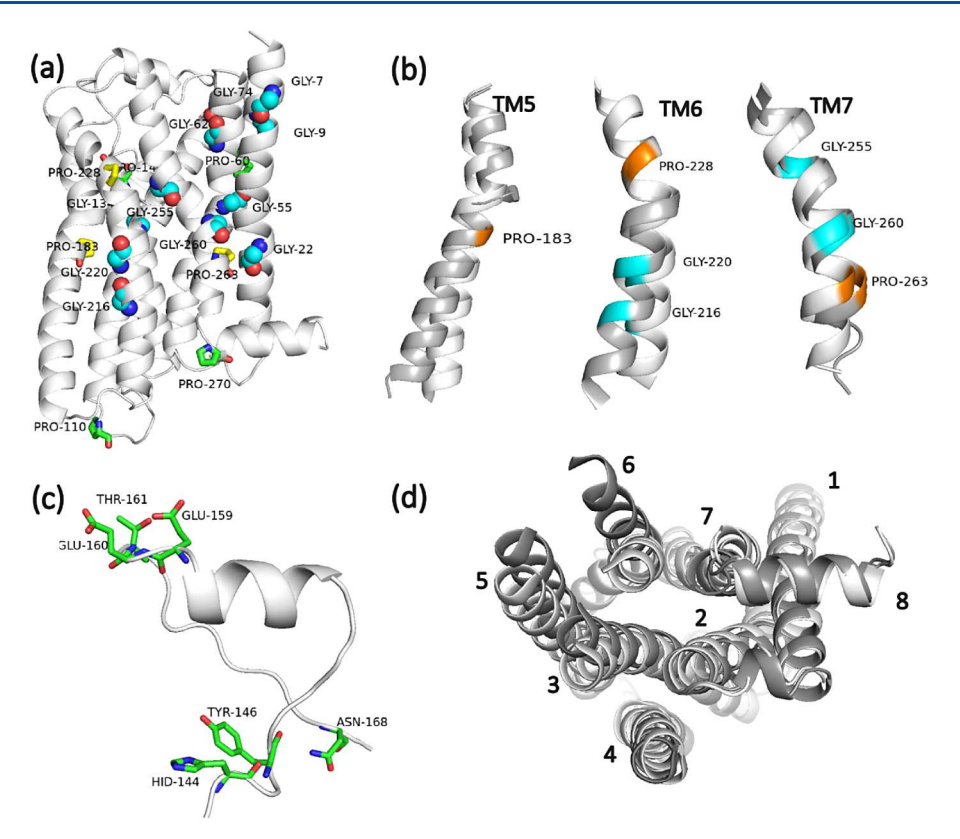


Figure 1. (a) Inactive state structure of β_2 AR. Glycines and prolines are shown as spheres and sticks, respectively, and prolines in motifs are shown in yellow. (b) Kink formation due to proline (orange) or glycine (cyan) in TM5, TM6, and TM7. The active state (dark gray) helices are overlaid to inactive state (light gray). (c) A portion of ECL2 discussed in the text. (d) Overlaying the active (dark gray) and inactive state (light gray), shown from the cytoplasmic side.

steady progress toward the development of more effective drugs to treat asthma using bronchodilators that are inhaled β_2 AR agonist ligands. Antagonist ligands of β_2 AR (β -blockers) are used for the treatment of cardiovascular disorders such as hypertension and angina. A detailed, residue-level free energy landscape of β_2 AR provides a representation for energy dynamics in this protein, accounting for the impact of agonist and antagonist ligands, shedding light on receptor dynamics, cell signaling, pharmacology, and protein engineering.

 β_2 AR consists of seven transmembrane (TM) helices, each connected by extracellular or intracellular loops, and another helix, helix 8, in the cytoplasm. ⁴⁵ Several prolines and glycines, which destabilize helices, ⁴⁹ facilitate the formation of kinks in TM5, TM6, and TM7, which contribute to GPCR flexibility and plasticity. ^{45,50–52} The kink in TM5 is formed by Pro183, in TM6 by Gly220, and in TM7 by Gly260. ⁵³ The locations of prolines and glycines are shown in Figure 1, as are the kinks in TM5 to TM7, and the structures of β_2 AR as seen from the cytoplasm.

2. COMPUTATIONAL METHODS

The disconnectivity graphs are generated from the complete set of rate constants for energy transfer between the amino acids of β_2 AR and the attached ligand, which are obtained from molecular dynamics (MD) simulations. The relative free energies depend on equilibrium occupation and hence the number of degrees of freedom and the size of the residues, while the lowest free energy barriers for energy to flow from a residue depend on the rate constants. By construction, the

stationary distribution is consistent with the equilibrium defined by the kinetics. The disconnectivity graph analysis reveals that bottlenecks to energy flow along β_2 AR, and probably other GPCRs, occur at glycines and prolines. Their role in energy transport along the main chain, and that of nearby noncovalent contacts in generating alternative pathways for energy flow are illustrated by computation of the first passage time (FPT) distributions for numerous selected energy sources and sinks. FPT distributions, like the disconnectivity graphs, are generated from the kinetic matrix by the full set of rate constants for energy transfer between the residues of β_2 AR to determine the relative probability for energy to flow from a source to a sink via all the possible pathways in a master equation representation. From the FPT distributions the mean first passage time (MFPT) between the source and sink is also computed. We find that the MFPT for transport along the main chain through a proline or glycine is longer than if neither of these residues is present over a comparable distance, and we compare MFPTs between sources and sinks for energy flow along the main chain and across noncovalent contacts.

We recently analyzed energy transport in β_2AR for the inactive and active states^{37,54} by computing energy currents between amino acid residues using data from MD simulations. Details of the MD simulations can be found in the Supporting Information. Using the position and velocity data, the CUrrent calculation for Proteins (CURP) version 1.2.1¹⁵ developed by Yamato and coworkers was used to calculate energy currents, G, between residue pairs from the energy flux time correlation function, as described in ref¹⁵. G is proportional to the rate of energy transfer, w, between residues. In previous work we

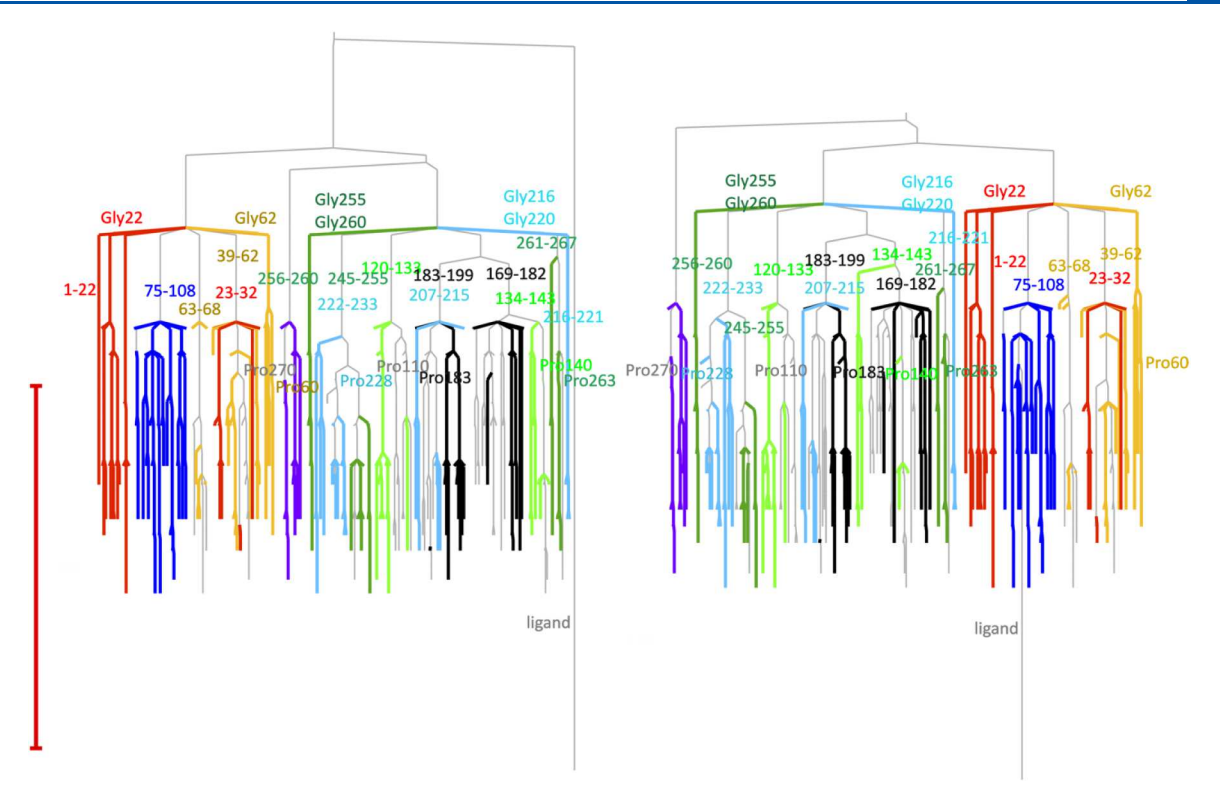


Figure 2. Disconnectivity graphs of β_2 AR in inactive (left) and active (right) states. The TM helices are colored red (TM1), orange (TM2), blue (TM3), light green (TM4), black (TM5), cyan (TM6), and dark green (TM7). Helix 8 is purple. The intracellular and extracellular loops connecting TM helices are shown in gray, as is the ligand. The residues belonging to the TM helices are labeled using the same color as the helix. Proline and glycine residues that create the barriers are labeled. The scale bar (left) is 1 kcal mol⁻¹.

computed G for all residues pairs of HP36.55 Rates of vibrational energy transfer, w, have also been computed from nonequilibrium simulations by Stock and coworkers. 10 On average, the value of G, which has units of $(kcal mol^{-1})^2 ps^{-1}$, can be converted to w using $w = G/(187 \text{ (kcal mol}^{-1})^2)$. We have used this conversion to produce rate constants from values of G for residue pairs of β_2 AR. The rate constants satisfy detailed balance, i.e., the rate of energy transfer from residue i with f_i degrees of freedom to j with f_i degrees of freedom, w_{ii} is $w_{ii} = w_{ii} (f_i/f_i)$. We note that some water molecules in the transmembrane region of GPCRs stabilize the active state, 56,57 and they can also provide pathways for energy transport. 56,58 The rate constants for energy transfer between residue pairs were computed with solvent molecules present, so the corresponding disconnectivity graphs account for the full system.

Disconnectivity graphs have been constructed to identify pathways for structural change in refs^{43,44,59-64} and were calculated as in ref ^{65,66} to identify pathways for vibrational energy flow in the space of amino acids and ligands. In this construction the relative free energies of the residues and the barriers between them are defined to reproduce the rates and the corresponding stationary distribution of the linear master equation. We compute FPT distributions, p(t), within the same master equation representation for energy transfer between all residue pairs following the procedure detailed in refs ^{65,67}. Dijkstra's algorithm⁶⁸ is applied to identify shortest paths between an energy source and sink. Here the metric for the path length is defined using edge weights $-\ln B_{ij}$, where B_{ij} is the branching probability from residue j to i. This choice selects the path corresponding to the largest term in the overall rate if intervening minima are treated in steady state.⁶⁹

3. RESULTS AND DISCUSSION

Disconnectivity graphs for the inactive and active states of β_2 AR are plotted in Figure 2. We discuss several prominent features of these graphs. First, we note that the energy scale of the lowest barriers separating minima is modest, of order 1 kcal mol⁻¹, consistent with the picosecond time scale for energy transfer between nearby amino acids. The relatively small barriers allow for facile flow of energy along the main chain of the protein. However, there is a noticeable variation in barrier heights, producing clusters of residues in the graph. Of the transmembrane helices only TM3 appears as a single cluster of residues. All other helices are fragmented into two or sometimes three clusters. TM1 and TM2, e.g., are each split into two clusters of residues. The first cluster contains residues of only one helix, and another is a mix of the two. Similar patterns are also found for TM4 to TM7. The grouping of different parts of helices will be discussed further below.

Residues of helix 8, which lies in the intracellular region, are clustered together. There is a significant barrier between helix 8 and the rest of the protein in both the inactive and active states, higher in active, which is due to Pro270 in the loop between TM7 and helix 8. We shall see that prolines generally produce bottlenecks to energy transfer along the main chain. The barrier is lower in the inactive state because on average there is more contact between helix 8 and other parts of the protein, in particular TM1, in that state.^{37,54} There is also a significant free energy barrier between helices 1–3 and helices 4–7, which is larger in the inactive state. This relatively high barrier is due to Pro110 in intercellular loop 2, ICL2. It is lower in the active state due to some contacts between helices toward the extracellular region that form in the active state and

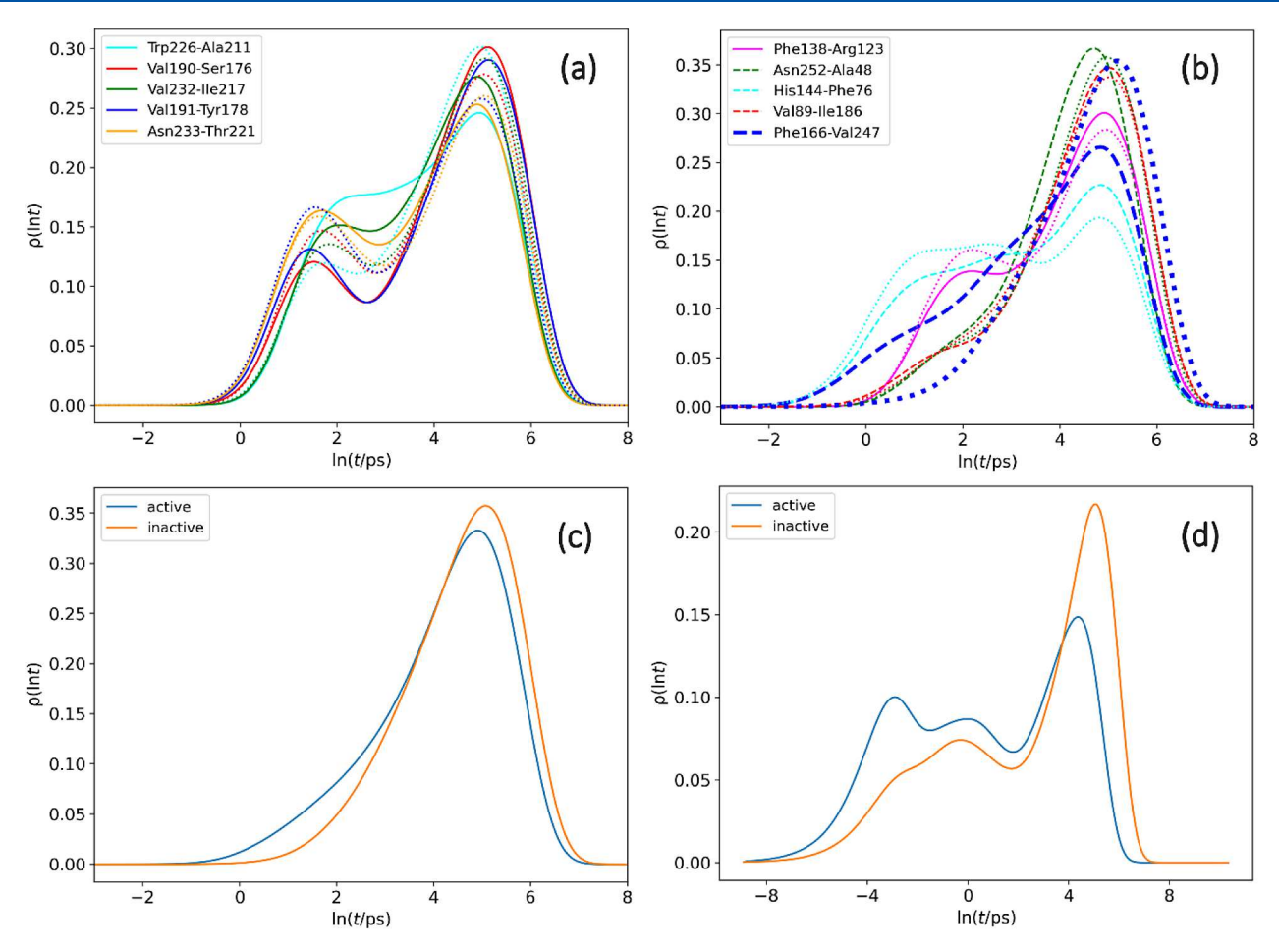


Figure 3. FPT distribution as a function of time, t (ps), plotted as $\rho(\ln t)$ vs $\ln t$, for (a) source-sink combinations in the same helix in active (solid) and inactive (dotted) states; (b) source-sink combinations in different helices in active (dashed) and inactive (dotted) states, apart from Phe138-Arg123 (magenta), both located in TM4. (c) Source-sink combination, Trp130-Ala170, in different helices with a fast shortcut channel in the active state due to small fluctuations in contact length, but slow transfer in the inactive state due to large fluctuations. (d) Ligand-Asp85 source-sink combination. $\rho(\ln t)$ is the probability distribution for the natural logarithm of the first passage time, t.

are absent or weaker in the inactive state, some of which will be discussed below.

We see throughout that prolines impede the flow of energy along the protein backbone. Several transmembrane helices, including TM5, TM6, and TM7 have a proline residue, specifically Pro183, Pro226, and Pro263, respectively. TM5 contains a sizable barrier due to Pro183, which separates the helix into two groups of residues in the graph. Structurally, Pro183 generates a kink in TM5 (see Figure 1). In addition to the prolines contained within TM5, TM6 and TM7, there are also prolines near the ends of TM2 and TM4. TM3 does not have a proline and appears as one unfragmented cluster of branches (blue).

Glycine, which like proline destabilizes helices, also creates significant barriers in the landscape for energy flow. TM1 appears fragmented in the disconnectivity graph due to Gly22, which breaks TM1 into two groups of branches, residues 1–22 and 23–32. When there is such fragmentation along the helix, the residues belonging to one of the clusters of branches can interact with other helices via a shortcut channel, i.e., a relatively strong noncovalent contact between the helices. Ile19 and Asn23 of TM1, both near Gly22, interact with Asp51 of TM2 creating a channel between TM1 and TM2. Gly62 fragments TM2 into two clusters of residues, 39–62 and 63–68.

The presence of both glycine and proline in a helix can also lead to fragmentation into different clusters of branches, as seen for TM4, which splits into three clusters due to Gly134 and Pro140, breaking up the helix into residues 120–133, 134–139, and 140–143. TM6 fragments due to two glycines and one proline, yielding 4 clusters of branches. TM7 also has two glycines and one proline which break it up into three groups of branches, residues 245–255, 256–260, and 261–267. Because Gly260 and Pro262 are very close in sequence the split occurs around 261.

In addition to the barrier in the energy landscape along the helices due to the presence of proline or glycine, residues next to proline or glycine often interact via relatively large noncovalent contacts with residues of other helices, generating alternative pathways for energy to flow. Such interactions are found between TM6-TM7, as Trp226-Gly255 and at Asn233-Tyr248. TM6 is seen to fragment from Asn233, giving rise to branches between Phe222-Asn233 and Ile234-Ile238. There are also noncovalent contacts between TM5-TM6, notably Ser176-Asn233, which facilitate energy transfer between the two helices. The contact Tyr181-Phe230 facilitates interaction between TM5 and TM6 above the kink in each helix.

Finally, we note that there is a deep well and small barrier between the agonist ligand, plotted as residue 283, and a cluster of residues near Asp85 in the active state, with which

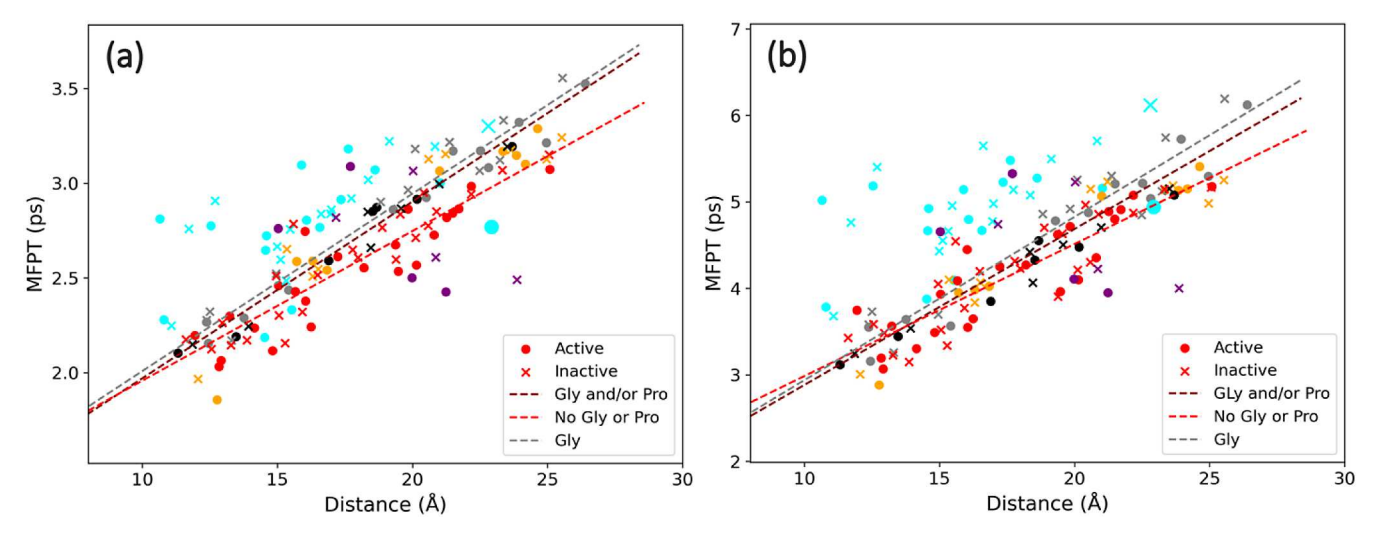


Figure 4. Mean first passage time (MFPT) for observation time t_{obs} of (a) 5 ps and (b) 10 ps vs center of mass distance between source and sink combinations. The cyan points represent combinations in different helices where a short-cut via a strong noncovalent interaction is present in at least one state. The other colors correspond to combinations in the same helix, with glycine between source and sink (gray), proline in between (black), both proline and glycine in between (orange), and neither glycine nor proline in between (red). The red line is a linear fit to red points, the gray line is a linear fit to gray points and the maroon line is a linear fit to gray, orange, and black points. Purple indicates the combinations belonging to the extracellular loop 2, ECL2.

the ligand interacts strongly. In the inactive state there is a relatively high barrier between the antagonist ligand and Asp85 and other residues due to weak interactions with the binding pocket.

We turn now to FPT distributions for energy flow between various energy source and sink combinations to illustrate the nature and rate of energy transport along helices, the role of prolines and glycines in that process, and to compare with energy flow between helices via noncovalent contacts. In Figure 3 we plot FPT distributions for selected source-sink combinations indicated in the figure. The distributions for all source-sink combinations exhibit at least one peak, with a most probable value of the order 100 ps, which is seen in all the FPT distributions we have computed. This peak arises from the random flow of energy among 283 chemical groups, the 282 amino acids and the ligand, and is not related to the structure of the disconnectivity graph, which is based on the lowest free energy pathways between residues. It apparently takes around 100 ps to pass through a residue, to the sink, at random, which is much longer than the time for excess vibrational energy to relax into the environment of the protein, as discussed below. We focus on peaks that appear at shorter times, corresponding to the faster pathways for energy flow revealed by the disconnectivity graphs.

FPT distributions for sources and sinks on the same helix, plotted in Figure 3a, exhibit two peaks for each combination plotted, one corresponding to a most probable time between 1 and 10 ps, and the other of order 100 ps, already discussed. FPT distributions for energy flow along a helix over lengths of at least 10 Å appear like the ones plotted in Figure 3a, each with two peaks that are typically similar for both active and inactive states. One exception is the source-sink combination Trp226-Ala211, along TM6. In the active state there is an opening of TM6 outward forming a sharper kink between Trp226 and Ala211 (Figure 1b), leading to a shift to longer times upon activation.

In Figure 3b we plot FPT distributions for source-sink combinations in different helices and compare with a source-

sink combination in the same helix. The FPT distribution for the latter case looks very much like those plotted in Figure 3a in both states. Interestingly, the distributions for source-sink combinations in different helices also appear like those in the same helix when there is a shortcut due to a strong noncovalent interaction between them. Among the curves plotted in Figure 3b are the FPT distributions for the source-sink combination Phe166-Val247 in active and inactive states, highlighted as thicker curves. This combination is located between ICL2 and TM7, and connected via Asp164-Lys245, which forms a polar contact in the active state. This contact is broken in the transition to the inactive state. We see a fast peak for the active state due to the short cut, but notably, none in the inactive state.

In Figure 3c, we plot FPT distributions for a source-sink combination, Trp130-Ala170, that passes through a contact, Thr136-Tyr171, which is intact in both the active and inactive states.³⁷ The contact exhibits small fluctuations in length in the active state and large fluctuations in the inactive state. Because of the small fluctuations in the active state, energy transfer through the contact is much faster than in the inactive state.³⁷ Because of the rapid rate of energy transfer through this contact we find, from the fastest path calculation using Dijkstra's algorithm, that energy transport from the source to the sink occurs via this contact in the active state. However, in the inactive state, because of the large fluctuations in the length of the contact and correspondingly slow rate of energy transfer, the fastest path from source to sink occurs via a different, neighboring contact. The difference in the FPT distributions for the two states is striking. There is a long tail, corresponding to a second peak in the distribution at shorter times, of order 1 to 10 ps, for the active state, with no such peak or shoulder for the inactive state.

When the source and sink are near one another we generally find three peaks in the FPT distribution. In Figure 3d we illustrate FPT distributions for the ligand as energy source and Asp85, the residue to which it is most closely in contact, as energy sink. Three peaks appear for both states, with the

shortest-time peak at roughly 0.05 ps, the middle peak near 1 ps, and a peak at times of order 100 ps. In the active state the peak near 0.05 ps is much higher and appears at shorter time. This difference reflects the stronger interaction between Asp 85 and the agonist ligand compared to the antagonist. The fast peak corresponds to direct energy transfer from the ligand to Asp85, while the peak near 1 ps corresponds to transitions between nearby residues between positions 83 and 86, and finally Asp85. The substantially higher barrier impeding the flow of energy between the antagonist and Asp85 is also apparent in Figure 2, where we see that the ligand is well separated from all branches of the disconnectivity graph in the inactive state, while it is well connected with residues of TM3 in the active state.

MFPTs are calculated from the FPT distribution, p(t), as the integral of tp(t) up to specific observation times, t_{obs} , following ref 67. Accounting explicitly for t_{obs} deals with limitations in the time over which vibrational energy transport between a source and sink can be measured in an experiment. Perhaps the most important limitation is the time for excess vibrational energy in the protein to relax to the environment, which may take roughly 5 or 10 ps. $^{9,10,70-72}$ The MFPT is generally expected to increase with distance between source and sink.

We plot MFPTs for selected source-sink combinations as a function of average center-of-mass distance between them in Figure 4, using observation times of (a) 5 ps and (b) 10 ps. The MFPTs plotted are also listed in the SI. MFPTs for source-sink combinations in different helices are shown in cyan. Results for these combinations are compared with MFPTs computed for source-sink combinations in the same helix. If there is a glycine between the source and sink in the sequence then the MFPT is plotted in gray; if there is a proline in the sequence the MFPT is plotted in black, and if there is both a proline and a glycine the MFPT is plotted in orange. If there is no proline or glycine in the sequence between the source and sink, the MFPT is plotted in red.

We see, as expected, that the MFPT increases with greater distance between source and sink. For energy transport along a helix the MFPT is often smaller for a given distance between source and sink than for energy transport between helices, but comparable to MFPTs for energy transport along the helix when there is fast energy transfer across a noncovalent contact. This effect is particularly noticeable for shorter observation times, because the peak at short times in the FPT distribution is often larger for energy transport along a helix than between helices.

For the source-sink combination Trp130-Ala170, in different helices, the MFPTs are plotted in cyan using a larger symbol in both active and inactive states. For this combination we see that, for its distance of around 23 Å, the MFPT in the active state is much shorter than MFPTs for flow along helices, particularly when the observation time is 5 ps, a time that is experimentally relevant.⁷² The short-cut in the active state is Thr136-Tyr171, which in this state exhibits only small fluctuations around its average length so that the rate constant for energy transfer between these residues is relatively large.³⁷ In the inactive state, as noted above, the contact remains intact, but distance fluctuations are relatively large and the rate constant for energy transfer is low.³⁷ We therefore find a large MFPT for this 23 Å distance between source and sink for the active state and a substantially smaller MFPT for the inactive state.

Linear fits to MFPTs for source-sink combinations in the same helix without a glycine or proline between them are plotted as red lines, combinations with a glycine in between as gray lines, and combinations that have a glycine, proline, or both as the maroon lines. The gray and maroon lines plotted in Figure 4a have slopes of 0.094 ps/Å and 0.093 ps/Å, respectively, and the red line has a slope of 0.079 ps/Å. In Figure 4b the gray, maroon, and red lines have slopes of 0.188 ps/Å, 0.180 ps/Å, and 0.153 ps/Å, respectively. These results confirm that the presence of a glycine or proline in a helix impedes energy transport. For the 5 ps observation time this conclusion holds to within the error in the fits for distances beyond around 20 Å, and for the 10 ps observation time it holds to within the error bars at distances beyond about 25 Å (see Supporting Information).

The time for energy transport along a helix, as determined by the MFPT and the distance between the source and sink, depends on observation times that are limited by relaxation of energy into the environment. For a 10 ps observation time, the rate of transport along a helix is on average 6.5 Å ps⁻¹ when no glycine or proline is present and falls to 5.4 Å ps⁻¹ if either a glycine or proline is present. For a 5 ps observation time, the rate of transport is on average 12.7 Å ps⁻¹ when no glycine or proline is present and is otherwise 10.6 Å ps⁻¹. These rates can be compared with the speed of sound in a protein, which has been computed⁷³ and measured⁷⁴ to be about 20 Å ps⁻¹. For shorter observation times a larger contribution of faster, more ballistic-like transport occurs, and we see that the speed of sound limit is approached in this case.

The data plotted in purple represent MFPTs for source-sink combinations located in ECL2 between TM4 and TM5. These combinations yield MFPTs that in some cases appear to be much faster than values along helices. In particular, the Glu160-Asn168 and Glu159-Asn168 source-sink combinations exhibit what appear to be very fast MFPTs for their respective center-of-mass distances. The His144-Thr161 and Tyr146-Glu159 source-sink combinations exhibit significantly longer MFPTs for similar center-of-mass distances. While the centerof-mass distances in the faster combinations are in fact slightly greater than the slower ones, they are just 7 or 8 positions apart along the sequence, since this part of ECL2 is relatively straight (Figure 11c). The slower combinations are separated by 15 to 17 residues in sequence, because this part of ECL2 is more crumpled in appearance (Figure 11c). There is thus more variability in MFPTs around a given center-of-mass distance for source-sink combinations that lie in coiled regions than for helices.

4. CONCLUSIONS

In summary, we have constructed and analyzed disconnectivity graphs to provide the first graphical representation of the vibrational energy landscape for a protein, in this study β_2AR , a rhodopsin-like GPCR, in its active and inactive states. The graphs are based on the relative free energy of each residue and the minimum free energy barriers for energy transfer between them, which are defined in terms of the rate constants for energy transfer between all pairs of amino acids and ligands. GPCRs consist of seven transmembrane helices and loops in the extra- and intracellular regions and the disconnectivity graphs reveal the nature of energy flow through these structural elements. Helices without either a proline or glycine are represented by a cluster of residues among which energy transport is facile, while helices with glycine or proline appear

fragmented, with separate clusters of residues on either side of the proline or glycine, grouped with residues from other helices when there are sizable noncovalent interactions between them. An important reason for the bottleneck to energy flow is their impact on the peptide structure. Both glycines and prolines destabilize helices⁴⁹ and contribute to their plasticity in GPCRs. 45,52 This effect alters the hydrogen bonding structure of the helix, which changes the energy flow.⁵⁵ The prolines form a five-membered cyclic ring, which results in the formation of a sharp kink in the peptide structure (see Figure 1). These structural differences as well as the relatively small number of degrees of freedom associated with these residues, particularly glycine, create a barrier to energy flow along the peptide chain. The effect of prolines and glycines on energy flow, and the emergence of competing pathways via noncovalent contacts near them, have been further quantified in this study by analysis of FPT distributions and the MFPTs computed with them.

Differences in energy transfer rates across noncovalent contacts in active and inactive states exhibit different organization in the vibrational landscape, as we see, for example, in the heights of minimum energy barriers between TM1-3 and TM 4-7, and between helix 8 and TM helices. These changes occur because a contact is broken or formed during the change in state, or because of changes in the dynamics of a contact, where fluctuations in the contact distance are smaller in one state than the other. Both effects, which contribute to allostery, give rise to qualitatively different FPT distributions for the two states when the contact lies between the energy source and sink.

Our results provide new insight into relations between composition, structure and energy dynamics of proteins that have evolved to perform tasks, such as signaling, which depend on these properties. There are implications for our understanding of allosteric transitions, and potential future applications to protein engineering and drug discovery. The present approach identifying residues that mediate rates of energy transfer is complementary to recent work computing structural correlations between residues, which was applied to elucidate allosteric regulation via communication between distant sites in the RNA-dependent ATPase/helicase Brr2.75 Both methods exploit MD simulations to analyze protein dynamics and infer functional relationships, including possible allosteric effects. Structural correlations can be used to construct a cross-correlation matrix, for which principal component analysis and community detection indicate the presence of dynamical coupling, which can be modulated by allosteric regulators.⁷⁵ In contrast, the focus in our approach is the matrix of energy transfer rates, which we use to visualize the organization of the corresponding free energy landscape and to calculate first passage time distributions between any pair of residues. This analysis reveals energy transfer across all the possible time scales for the molecule and has yielded insights into specific residues that mediate energy flow in β_2 AR. The free energy landscape provides a representation governing the flow of energy that is measured in time-resolved vibrational spectroscopic experiments, which probe the dynamical response of a protein to local excitation and chemical reaction. The impact of prolines and glycines on energy flow identified in this study, and their impact on the response of β_2 AR to agonist and antagonist binding, provide predictions that can be tested by vibrational spectroscopy. In future work it would be interesting to carry out dynamical

network and community analysis on β_2 AR, as recently applied to Brr2, 75 to further elucidate the impact of the agonist and antagonist on the dynamics.

ASSOCIATED CONTENT

Supporting Information

The Supporting Information is available free of charge at https://pubs.acs.org/doi/10.1021/acs.jpcb.4c04513.

List of source-sink combinations, complete set of rate constants on GitHub, and fits of first mean passage times and error bars (PDF)

AUTHOR INFORMATION

Corresponding Authors

David J. Wales – Yusuf Hamied Department of Chemistry, Cambridge University, Cambridge CB2 1EW, U.K.; Email: dw34@cam.ac.uk

David M. Leitner — Department of Chemistry, University of Nevada, Reno, Nevada 89557, United States; ⊚ orcid.org/0000-0002-3105-818X; Email: dml@unr.edu

Author

Humanath Poudel – Department of Chemistry, University of Nevada, Reno, Nevada 89557, United States

Complete contact information is available at: https://pubs.acs.org/10.1021/acs.jpcb.4c04513

Notes

The authors declare no competing financial interest.

ACKNOWLEDGMENTS

Support from NSF grant CHE-2245240 (DML) is gratefully acknowledged.

REFERENCES

- (1) Baumann, T.; Hauf, M.; Schildhauer, F.; Eberl, K. B.; Durkin, P. M.; Deniz, E.; Löffler, J. G.; Acevedo-Rocha, C. G.; Jaric, J.; Martins, B. M.; et al. Observation of Site-Resolved Vibrational Energy Transfer Using a Genetically Encoded Ultrafast Heater. *Angew. Chem.* **2019**, 58, 2899–2903.
- (2) Deniz, E.; Valiño-Borau, L.; Löffler, J. G.; Eber, K. B.; Gulzar, A.; Wolf, S.; Durkin, P. M.; Kaml, R.; Budisa, N.; Stock, G.; et al. Through Bonds or Contacts? Mapping Protein Vibrational Energy Transfer Using Non-Canonical Amino Acids. *Nat. Commun.* **2021**, *12*, 3284.
- (3) Fujii, N.; Mizuno, M.; Ishikawa, H.; Mizutani, Y. Observing Vibrational Energy Flow in a Protein with the Spatial Resolution of a Single Amino Acid Residue. *J. Phys. Chem. Lett.* **2014**, *5*, 3269–3273.
- (4) Kondoh, M.; Mizuno, M.; Mizutani, Y. Importance of Atomic Contacts in Vibrational Energy Flow in Proteins. *J. Phys. Chem. Lett.* **2016**, *7*, 1950–1954.
- (5) Yamashita, S.; Mizuno, M.; Tran, D. P.; Dokainish, H.; Kitao, A.; Mizutani, Y. Vibrational Energy Transfer from Heme through Atomic Contacts in Proteins. *J. Phys. Chem. B* **2018**, *122*, 5877–5884.
- (6) Mizutani, Y.; Mizuno, M. Time-Resolved Spectroscopic Mapping of Vibrational Energy Flow in Proteins: Understanding Thermal Dffusion at the Nanoscale. *J. Chem. Phys.* **2022**, *157*, 240901.
- (7) Leitner, D. M. Energy Flow in Proteins. Annu. Rev. Phys. Chem. **2008**, 59, 233–259.
- (8) Leitner, D. M.; Straub, J. E. Proteins: energy, Heat and Signal Flow; CRC Press, Taylor & Francis Group: Boca Raton, FL, 2010.
- (9) Leitner, D. M.; Buchenberg, S.; Brettel, P.; Stock, G. Vibrational Energy Flow in the Villin Headpiece Subdomain: Master Equation Simulations. *J. Chem. Phys.* **2015**, *142*, 075101.

- (10) Buchenberg, S.; Leitner, D. M.; Stock, G. Scaling Rules for Vibrational Energy Transport in Globular Proteins. *J. Phys. Chem. Lett.* **2016**, *7*, 25–30.
- (11) Bu, L.; Straub, J. E. Simulating Vibrational Energy Flow in Proteins: Relaxation Rate and Mechanism for Heme Cooling in Cytochrome C. J. Phys. Chem. B 2003, 107, 12339–12345.
- (12) Leitner, D. M. Frequency Resolved Communication Maps for Proteins and Other Nanoscale Materials. *J. Chem. Phys.* **2009**, *130*, 195101.
- (13) Leitner, D. M.; Yamato, T. Mapping Energy Transport Networks in Proteins. In *Reviews in Computational Chemistry*, Parrill, A. L.; Lipkowitz, K. B., Eds.; John Wiley & Sons, Inc., 2018; Vol. 31, pp. 63114.
- (14) Leitner, D. M.; Yamato, T. Recent Developments in the Computational Study of Protein Structural and Vibrational Energy Dynamics. *Biophys. Rev.* **2020**, *12*, 317–322.
- (15) Ishikura, T.; Iwata, Y.; Hatano, T.; Yamato, T. Energy Exchange Network of Inter-Residue Interactions within a Thermally Fluctuating Protein: A Computational Study. *J. Comput. Chem.* **2015**, *36*, 1709–1718
- (16) Ishikura, T.; Yamato, T. Energy Transfer Pathways Relevant for Long-Range Intramolecular Signaling of Photosensory Protein Revealed by Microscopic Energy Conductivity Analysis. *Chem. Phys. Lett.* **2006**, 432, 533–537.
- (17) Ota, K.; Yamato, T. Energy Exchange Network Model Demonstrates Protein Allosteric Transition: An Application to an Oxygen Sensor Protein. *J. Phys. Chem. B* **2019**, *123*, 768–775.
- (18) Sagnella, D. E.; Straub, J. E. Directed Energy "Funneling" Mechanism for Heme Cooling Following Ligand Photolysis or Direct Excitation in Solvated Carbonmonoxy Myoglobin. *J. Phys. Chem. B* **2001**, *105*, 7057–7063.
- (19) Sagnella, D. E.; Straub, J. E.; Jackson, T. A.; Lim, M.; Anfinrud, P. A. Vibrational Population Relaxation of Carbon Monoxide in the Heme Pocket of Carbonmonoxy Myoglobin: Comparison of Time-Resolved Mid-Ir Absorbance Experiments and Molecular Dynamics Simulations. *Proc. Natl. Acad. Sci. U. S. A.* 1999, 96, 14324–14329.
- (20) Nagy, A. M.; Raicu, V.; Miller, R. J. D. Nonlinear Optical Studies of Heme Protein Dynamics: Implications for Proteins as Hybrid States of Matter. *Biochim. Biophys. Acta* **2005**, *1749*, 148–172.
- (21) Mizutani, Y.; Kitagawa, T. Direct Observation of Cooling of Heme Upon Photodissociation of Carbonmonoxy Myoglobin. *Science* **1997**, 278, 443–446.
- (22) Henry, E. R.; Eaton, W. A.; Hochstrasser, R. M. Molecular Dynamics Simulations of Cooling in Laser-Excited Heme Proteins. *Proc. Natl. Acad. Sci. U. S. A.* **1986**, *83*, 8982–8986.
- (23) Hamm, P.; Lim, M.; Hochstrasser, R. M. Structure of the Amide I Band of Peptides Measured by Fs Nonlinear-Infrared Spectroscopy. *J. Phys. Chem. B* **1998**, *102*, 6123–6138.
- (24) Lian, T.; Locke, B.; Kholodenko, Y.; Hochstrasser, R. M. Energy Flow from Solute to Solvent Probed by Femtosecond IR Spectroscopy: Malachite Green and Heme Protein Solutions. *J. Phys. Chem.* **1994**, *98*, 11648–11656.
- (25) Helmer, N.; Wolf, S.; Stock, G. Energy Transport and Its Function in Heptahelical Transmembrane Proteins. *J. Phys. Chem. B* **2022**, *126*, 8735–8746.
- (26) Valino-Borau, L.; Gulzar, A.; Stock, G. Master Equation Model to Predict Energy Transport Pathways in Proteins. *J. Chem. Phys.* **2020**, *152*, 045103.
- (27) Fujisaki, H.; Straub, J. E. Vibrational Energy Relaxation of Isotopically Labeled Amide I Modes in Cytochrome C: Theoretical Investigation of Vibrational Energy Relaxation Rates and Pathways. *J. Phys. Chem. B* **2007**, *111*, 12017–12023.
- (28) Poudel, H.; Leitner, D. M. What Measurements of Energy Transfer across Non-Covalent Contacts in Proteins Reveal About the Energy Landscape. *I. Innov. Mater. Extreme Cond.* **2024**, *5*, 45–56.
- (29) Yamato, T.; Wang, T.; Sugiura, W.; Laprevote, O.; Katagiri, T. Computational Study on the Thermal Conductivity of a Protein. *J. Phys. Chem. B* **2022**, *126*, 3029–3036.

- (30) Kozlowski, R.; Zhao, J.; Dyer, R. B. Acceleration of Catalysis in Dihydrofolate Reductase by Transient, Site-Specific Photothermal Excitation. *Proc. Natl. Acad. Sci. U. S. A.* **2021**, *118*, No. e2014592118.
- (31) Zaragoza, J. P. T.; Offenbacher, A. R.; Hu, S.; Gee, C. L.; Firestein, Z. M.; Minnetian, N.; Deng, Z.; Fan, F.; Iavarone, A. T.; Klinman, J. P. Temporal and Spatial Resolution of Distal Protein Motions That Activate Hydrogen Tunneling in Soybean Lipoxygenase. *Proc. Natl. Acad. Sci. U. S. A.* 2023, 120, No. e2211630120.
- (32) Ohler, A.; Taylor, P. E.; Bledsoe, J. A.; Iavarone, A. T.; Gilbert, N. C.; Offenbacher, A. R. Identification of the Thermal Activation Network in Human 15-Lipoxygenase-2: Divergence from Plant Orthologs and Its Relationship to Hydrogen Tunneling Activation Barriers. ACS Catal. 2024, 14, 5444–5457.
- (33) Gao, S.; Klinman, J. P. Functional Roles of Enzyme Dynamics in Accelerating Active Site Chemistry: Emerging Techniques and Changing Concepts. *Curr. Opin. Struct. Biol.* **2022**, *75*, 102434.
- (34) Schoenlein, R. W.; Peteanu, L. A.; Mathies, R. A.; Shank, C. V. The First Step in Vision: Femtosecond Isomerization of Rhodopsin. *Science* 1721, 254, 412–415.
- (35) Kukura, P.; McCamant, D. W.; Yoon, S.; Wandschneider, D. B.; Mathies, R. A. Structural Observation of the Primary Isomerization in Vision with Femtosecond-Stimulated Raman. *Science* **2005**, *310*, 1006–1009.
- (36) Kim, J. E.; Tauber, M. J.; Mathies, R. A. Analysis of the Mode-Specific Excited-State Energy Distribution and Wavelength-Dependent Photoreaction Quantum Yield in Rhodopsin. *Biophys. J.* **2003**, *84*, 2492–2501.
- (37) Poudel, H.; Leitner, D. M. Locating Dynamic Contributions to Allostery Via Determining Rates of Vibrational Energy Transfer. *J. Chem. Phys.* **2023**, *158*, 015101.
- (38) Reid, K. M.; Yamato, T.; Leitner, D. M. Scaling of Rates of Vibrational Energy Transfer in Proteins with Equilibrium Dynamics and Entropy. *J. Phys. Chem. B* **2018**, *122*, 9331–9339.
- (39) Leitner, D. M.; Pandey, H. D.; Reid, K. M. Energy Transport across Interfaces in Biomolecular Systems. *J. Phys. Chem. B* **2019**, *123*, 9507–9524.
- (40) Reid, K. M.; Yamato, T.; Leitner, D. M. Variation of Energy Transfer Rates across Protein—Water Contacts with Equilibrium Structural Fluctuations of a Homodimeric Hemoglobin. *J. Phys. Chem. B* **2020**, *124*, 1148–1159.
- (41) Reid, K. M.; Yu, X.; Leitner, D. M. Change in Vibrational Entropy with Change in Protein Volume Estimated with Mode Grüneisen Parameters. *J. Chem. Phys.* **2021**, *154*, 055012.
- (42) Chen, K.-Y. M.; Keri, D.; Barth, P. Computational Design of G Protein-Coupled Receptor Allosteric Signal Transductions. *Nat. Chem. Biol.* **2020**, *16*, 77–86.
- (43) Becker, O. M.; Karplus, M. The Topology of Multidimensional Potential Energy Surfaces: Theory and Application to Peptide Structure and Kinetics. *J. Chem. Phys.* **1997**, *106*, 1495–1517.
- (44) Wales, D. J.; Miller, M. A.; Walsh, T. R. Archetypal Energy Landscpaes. *Nature* **1998**, 394, 758–760.
- (45) Rosenbaum, D. M.; Rasmussen, S. G.; Kobilka, B. K. The Structure and Function of G-Protein-Coupled Receptors. *Nature* **2009**, *459*, 356–363.
- (46) Waldeck, B. β -Adrenoceptor agonists and asthma—100 years of development. *Eur. J. Pharmacol.* **2002**, 445, 1–12.
- (47) Monaco, T. J.; Hanania, N. A. Emerging Inhaled Long-Acting Beta-2 Adrenoceptor Agonists for the Treatment of Copd. *Expert Opin. Emerging Drugs* **2017**, 22, 285–299.
- (48) Weber, M. A. The Role of the New B-Blockers in Treating Cardiovascular Disease. *Am. J. Hypertens.* **2005**, *18*, 169S–176S.
- (49) Pace, C. N.; Scholtz, J. M. A Helix Propensity Scale Based on Experimental Studies of Peptides and Proteins. *Biophys. J.* **1998**, *75*, 422–427.
- (50) VanArnam, E. B.; Lester, H. A.; Dougherty, D. A. Dissecting the Functions of Conserved Prolines within Transmembrane Helices of the D2 Dopamine Receptor. *ACS Chem. Biol.* **2011**, *6*, 1063–1068.
- (51) Mazna, P.; Grycova, L.; Balik, A.; Zemkova, H.; Friedlova, E.; Obsilova, V.; Obsil, T.; Teisinger, J. The Role of Proline Residues in

- the Structure and Function of Human Mt2Melatonin Receptor. *J. Pineal Res.* **2008**, *45*, 361–372.
- (52) Gan, X.; Ma, Z.; Deng, N.; Wang, J.; Ding, J.; Li, L. Involvement of the C-Terminal Proline-Rich Motif of G Protein-Coupled Receptor Kinases in Recognition of Activated Rhodopsin. *J. Biol. Chem.* **2004**, *279*, 49741–49746.
- (53) Hauser, A. S.; Kooistra, A. J.; Munk, C.; Heydenreich, F. M.; Veprintsev, D. B.; Bouvier, M.; Babu, M. M.; Gloriam, D. E. GPCR Activation Mechanisms across Classes and Macro/Microscales. *Nat. Struct. Mol. Biol.* **2021**, *28*, 879–888.
- (54) Poudel, H.; Leitner, D. M. Activation-Induced Reorganization of Energy Transport Networks in the B2 Adrenergic Receptor. *J. Phys. Chem. B* **2021**, *125*, 6522–6531.
- (55) Poudel, H.; Reid, K. M.; Yamato, T.; Leitner, D. M. Energy Transfer across Nonpolar and Polar Contacts in Proteins: Role of Contact Fluctuations. *J. Phys. Chem. B* **2020**, 124, 9852–9861.
- (56) Poudel, H.; Leitner, D. M. Energy Transport in Class B GPCRs: Role of Protein–Water Dynamics and Activation. *J. Phys. Chem. B* **2022**, *42*, 8362–8373.
- (57) Lee, Y.; Kim, S.; Choi, S.; Hyeon, C. Ultraslow Water-Mediated Transmembrane Interactions Regulate the Activation of A2a Adenosine Receptor. *Biophys. J.* **2016**, *111*, 1180–1191.
- (58) Leitner, D. M.; Hyeon, C.; Reid, K. M. Water-Mediated Biomolecular Dynamics and Allostery. *J. Chem. Phys.* **2020**, *152*, 240901.
- (59) Wales, D. J. Energy Landscapes; Cambridge University Press: Cambridge, 2003.
- (60) Czerminski, R.; Elber, R. Reaction Path Study of Conformational Transitions and Helix Formation in a Tetrapeptide. *Proc. Natl. Acad. Sci. U. S. A.* **1989**, *86*, 6963–6967.
- (61) Baba, A.; Komatsuzaki, T. Construction of Effective Free Energy Landscape from Single-Molecule Time Series. *Proc. Natl. Acad. Sci. U. S. A.* **2007**, *104*, 19297–19302.
- (62) Komatsuzaki, T.; Hoshino, K.; Matsunaga, Y.; Rylance, G. J.; Johnston, R. L.; Wales, D. J. How Many Dimensions Are Required to Approximate the Potential Energy Landscape of a Model Protein. *J. Chem. Phys.* **2005**, *122*, 084714.
- (63) Krivov, S. V.; Karplus, M. Free Energy Disconnectivity Graphs: Application to Peptide Models. *J. Chem. Phys.* **2002**, *117*, 10894–10903
- (64) Evans, D. A.; Wales, D. J. Free Energy Landscapes of Model Peptides and Proteins. *J. Chem. Phys.* **2003**, *118*, 3891–3897.
- (65) Woods, E. J.; Wales, D. J. Analysis and Interpretation of First Passage Time Distributions Featuring Rare Events. *Phys. Chem. Chem. Phys.* **2024**, 26, 1640–1657.
- (66) Woods, E. J.; Kannan, D.; Sharpe, D. J.; Swinburne, T. D.; Wales, D. J. Analysing Ill-Conditioned Markov Chains. *Phil. Trans. R. Soc. A* **2023**, 381, 20220245.
- (67) Wales, D. J. Dynamical Signatures of Multifunnel Landscapes. *J. Phys. Chem. Lett.* **2022**, *13*, 6349–6358.
- (68) Dijkstra, E. W. A Note on Two Problems in Connection with Graphs. *Numer. Math.* **1959**, *1*, 269–271.
- (69) Wales, D. J. Discrete Path Sampling. Mol. Phys. 2002, 100, 3285-3305.
- (70) Nguyen, P. H.; Park, S. M.; Stock, G. Nonequilibrium Molecular Dynamics Simulation of the Energy Transfer through a Peptide Helix. *J. Chem. Phys.* **2010**, 132, 025102.
- (71) Nguyen, P. H.; Hamm, P.; Stock, G. Nonequilibrium Molecular Dynamics Simulation of Photoinduced Energy Flow in Peptides: Theory Meets Experiment. In *Proteins: Energy, Heat and Signal Flow,* Leitner, D. M.; Straub, J. E., Eds.; CRC Press, Taylor & Francis Group: Boca Raton, 2010; pp. 149168.
- (72) Botan, V.; Backus, E. H. G.; Pfister, R.; Moretto, A.; Crisma, M.; Toniolo, C.; Nguyen, P. H.; Stock, G.; Hamm, P. Energy Transport in Peptide Helices. *Proc. Natl. Acad. Sci. U. S. A.* **2007**, *104*, 12749–12754.
- (73) Yu, X.; Leitner, D. M. Vibrational Energy Transfer and Heat Conduction in a Protein. J. Phys. Chem. B 2003, 107, 1698–1707.

- (74) Levantino, M.; Schiro, G.; Lemke, H. T.; Cottone, G.; Glownia, J. M.; Zhu, D.; Chollet, M.; Ihee, H.; Cupane, A.; Cammarata, M. Ultrafast Myoglobin Structural Dynamics Observed with an X-Ray Free-Electron Laser. *Nat. Commun.* **2015**, *6*, 6772.
- (75) Mattioli, F. G.; Saltalamacchia, A.; Magistrato, A. Tracing Allostery in the Spliceosome Ski2-Like RNA Helicase Brr2. *J. Phys. Chem. Lett.* **2024**, *15*, 3502–3508.